

X-ray diagnostics of Cassiopeia A’s “Green Monster”: evidence for dense shocked circumstellar plasma

JACCO VINK,^{1,2} MANAN AGARWAL,¹ PATRICK SLANE,³ ILSE DE LOOZE,⁴ DAN MILISAVLJEVIC,^{5,6} DANIEL PATNAUDE,³ AND TEA TEMIM⁷

¹ Anton Pannekoek Institute/GRAPPA, University of Amsterdam, Science Park 904, 1098 XH Amsterdam, The Netherlands

² SRON Netherlands Institute for Space Research, Niels Bohrweg 4, 2333 CA Leiden, The Netherlands

³ Center for Astrophysics | Harvard & Smithsonian, 60 Garden Street, Cambridge, MA 02138, USA

⁴ Sterrenkundig Observatorium, Ghent University, Krijgslaan 281 - S9, B-9000 Gent, Belgium

⁵ Purdue University, Department of Physics and Astronomy, 525 Northwestern Ave, West Lafayette, IN 47907

⁶ Integrative Data Science Initiative, Purdue University, West Lafayette, IN 47907, USA

⁷ Princeton University, 4 Ivy Ln, Princeton, NJ 08544, USA

ABSTRACT

The recent survey of the core-collapse supernova remnant Cassiopeia A (Cas A) with the MIRI instrument on board the James Webb Space Telescope (JWST) revealed a large structure in the interior region, referred to as the “Green Monster”. Although its location suggests that it is an ejecta structure, the infrared properties of the “Green Monster” hint at a circumstellar medium (CSM) origin. In this companion paper to the JWST Cas A paper, we investigate the filamentary X-ray structures associated with the “Green Monster” using Chandra X-ray Observatory data. We extracted spectra along the “Green Monster” as well as from shocked CSM regions. Both the extracted spectra and a principal component analysis show that the “Green Monster” emission properties are similar to those of the shocked CSM. The spectra are well-fit by a model consisting of a combination of a non-equilibrium ionization model and a power-law component, modified by Galactic absorption. All the “Green Monster” spectra show a blueshift of around -2500 km s^{-1} , suggesting that the structure is on the near side of Cas A. The ionization age is around $n_e t \approx 1.4 \times 10^{11} \text{ cm}^{-3}\text{s}$. This translates into a pre-shock density of $\sim 11 \text{ cm}^{-3}$, higher than previous estimates of the unshocked CSM. The relatively high $n_e t$ and relatively low radial velocity suggest that this structure has a relatively high density compared to other shocked CSM plasma. This analysis provides yet another piece of evidence that the CSM around Cas A’s progenitor was not that of a smooth steady wind profile.

Keywords: Supernova remnants (1667) — X-ray astronomy (1810) — Stellar mass loss (1613) — Circumstellar dust(236)

1. INTRODUCTION

The infrared imaging mosaics based on the 2022 James Webb Space Telescope (JWST) observations with the MIRI and NIRCAM camera of the young core-collapse supernova remnant Cassiopeia A (Cas A) revealed in exquisite detail various spatial infrared (IR) components, such as numerous, small ejecta knots emitting thermal dust radiation, a more diffuse circumstellar medium (CSM) component in the outer shell, and, with NIRCAM, very diffuse emission likely caused by syn-

chrotron radiation (Milisavljevic et al. submitted).¹ These basic components were known from previous IR and multiwavelength observations, but unexpectedly the JWST images also revealed a giant loop structure across part of the interior of Cas A. This IR structure was popularized under the name the “Green Monster”. The location of this loop interior to the main shell seems to indicate an ejecta origin, but its filamentary structure is morphologically very distinct from the more prominent ejecta components, consisting of numerous small knots.

¹ See also the press release image of April 7, 2023, <https://www.nasa.gov/universe/webb-reveals-never-before-seen-details-in-cassiopeia-a>.

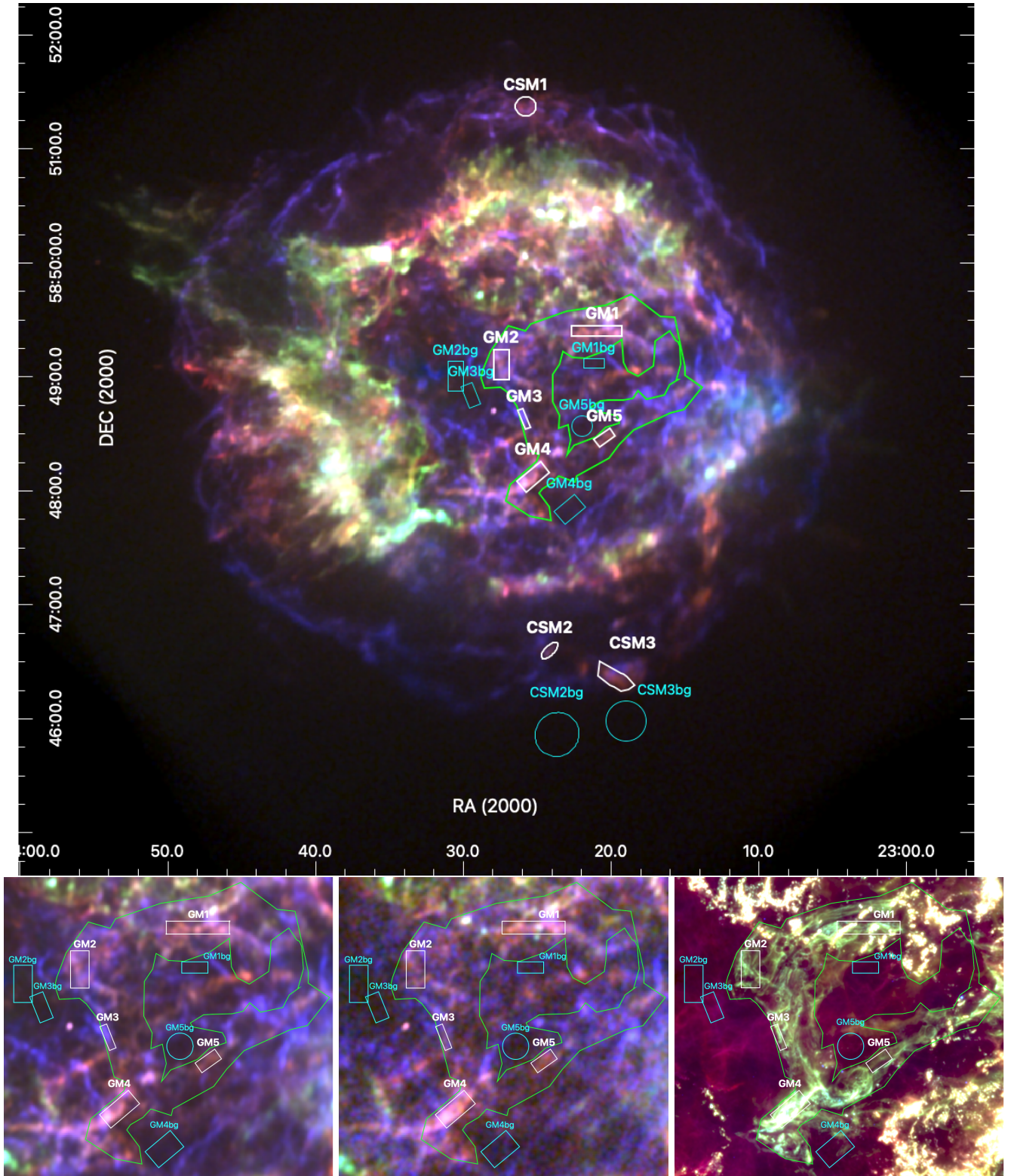


Figure 1. Top panel: RGB color image using the narrow bands 1.2–1.4keV (red, showing Fe-L and Mg XI line emission), 1.85–1.98 keV (green, Si XII), and 4.0–4.5keV (blue, continuum). The images are obtained by combining images from several individual deep observations in 2004 (ObsID 4634, 4635, 4636, 4637, 4638, 4723). The outline of the “Green Monster” structure is shown with green polygons. Spectral extraction regions along the “Green Monster” (GM 1–5) and three CSM-related structures (CSM 1–3) are shown in white. The background regions used are shown in cyan. Bottom panels: The central region of Cas A in X-rays in 2004 (left), 2019 (ObsID19606, center), and IR using JWST/MIRI data (right). The X-ray extraction regions are overlaid as well as a rough outline of the “Green Monster”. The RGB channels are for the X-ray images identical to those in the top panel. The JWST map consists of the F2550W (red), F1800W (green), and F1000W (blue) filters (see Milisavljevic et al.). All images employ square-root brightness scaling.

The IR properties of the “Green Monster” (GM) are somewhat similar to a large protrusion in the southern part, which is associated with a bright radio feature (e.g., feature H in Braun 1987), and with an arc of nitrogen-rich knots, labeled quasi-stationary flocculi (QSFs, van den Bergh 1971; Koo et al. 2020). See the labeling in Fig. A1. The spectra of these QSFs show that they find their origin in the helium- and nitrogen-enriched wind of the progenitor star (e.g., Koo et al. 2023), and are hence associated with the CSM.

However, its locations and small “bullet-hole”-like features in the GM filaments prompted us to scrutinize the identification of the GM as a shocked CSM rather than an ejecta structure. This letter is a companion paper to the JWST results reported by Milisavljevic et al. — providing a general overview of Cas A observations by JWST— and the paper by De Looze et al., which focuses on the IR the morphology and spectroscopy of the GM. De Looze et al. report that the IR spectroscopic properties of the GM has similarities with those regions containing QSFs, and are spectroscopically distinct from other CSM-related dust emission. They attribute this to a high carbon-over-silicate grain abundance ratio for the GM/QSF regions, as compared to other CSM-related dust components.

Here we show that X-ray filaments associated with the GM do indeed have X-ray characteristics shared with shocked CSM. This analysis is based on archival X-ray data gathered by the NASA Chandra X-ray Observatory (Chandra for short).²

2. X-RAY DATA

2.1. *X-ray spectra of “Green Monster” region and the southern CSM*

Chandra X-ray Observatory observed Cas A numerous times with the ACIS-S CCD detectors in imaging mode. The last such observation concerned a 49ks deep exposure made in 2019 (ObsID 19606). Much deeper exposures—1 Ms in total, but individual exposure amounting to 170 ks—were made in 2004 as part of the Chandra very-large program (VLP) (Hwang et al. 2004).

The X-ray maps using an RGB color representation—see Fig. 1—reveal reddish filamentary structures that align well, but not perfectly, with the GM identified in the JWST maps (Fig. 1 lower right). The reddish color in the X-ray maps corresponds with the 1.2-1.4 keV band, which is characterized by Mg XI/XII, and Fe-L

line emission. The reddish color is in stark contrast to the greenish color associated with Si XII line emission from Si-rich ejecta, and the blue/purplish color of X-ray synchrotron radiation.

The RGB X-ray maps, therefore, already provide a hint that the X-ray emission associated with the GM is not associated with Si-rich ejecta, or synchrotron emission. In Fig. 1(top) two other components also appear red: the iron-rich ejecta in the southeastern region (Hughes et al. 2000; Hwang & Laming 2012), and a very bright red filament just above the base of the eastern jet, known as “Baade-Minkowski’s filament 1” (Baade & Minkowski 1954), which contains O/Ne/Mg rich ejecta (Vink 2004).

The morphology of these filaments show some evolution between 2004 and 2019 (c.f. Fig. 1 bottom left and center). In the north of the GM some stronger Si-lines show up in the 2019 data set, possibly coinciding with the regions of ejecta knots seen with JWST/MIRI in the northern part of the GM. In addition, the GM overlaps partially with nonthermal X-ray filaments, which seem to evolve relatively rapidly in some regions (Patnaude et al. 2011; Vink et al. 2022), causing some different spectral characteristics between 2004 and 2019. These nonthermal filaments are either associated with the forward shock (Gotthelf et al. 2001; Vink & Laming 2003), but projected to the interior, or they are associated with the reverse shock regions (Helder & Vink 2008; Uchiyama & Aharonian 2008), requiring relative speeds between the reverse shock and the unshocked ejecta of $\gtrsim 3000 \text{ km s}^{-1}$, a requirement that seems to met in parts of the western half of Cas A (Vink et al. 2022). Since the reddish-colored filaments associated with the GM itself are relatively stable between 2004 and 2019, we opted for an investigation of the deepest single observation run available, which is the 2004 observation labeled ObsID 4638. We found that the extracted spectra have good statistics, with most of the uncertainties arising from systematic effects, such as the choice (or discarding) of background spectra. The data were processed with the Chandra software package *ciao*-4.15, and employed the *xspec* package (Arnaud 1996) for spectral analysis.

We extracted five spectra along the GM filaments, as well as a region associated at the tip of the arc of QSFs (CSM3), a fainter region in the south, outside the ejecta shell (CSM2), and also associated with QSFs. For comparison we also extracted a relatively bright CSM region in the north (CSM1), with no QSF counterpart. Background spectra were obtained from faint nearby regions, assuming that the extracted spectra of filaments contain also more diffuse components plus other background components. We note here that even background spec-

² Extracted data products as well as software will be made available on <https://doi.org/10.5281/zenodo.10301088>

tra from extraction regions outside Cas A still seem to be dominated by dust scattered X-ray emission from Cas A itself. All extraction regions are displayed in Fig. 1. All the spectra were optimally binned following the procedure described in Kaastra & Bleeker (2016) through the FTool (Blackburn 1995) task `ftgrouppha`.

For fitting spectra, we experimented with both a model using the standard non-equilibrium ionization (NEI) model `vnei` and the `vpshock` model (Borkowski et al. 2001). The `vnei` assumes a single ionization age τ (or $n_e t$), whereas `vpshock` assumes a superposition of ionization ages assuming a plane parallel shock geometry. Since the `vpshock` is more realistic, we report here only the `vpshock` model fits. The `vpshock` model specifies a lower and an upper bound to the ionization age, τ_{\max} . The lower bound was set to zero, and the upper bound was left as a free parameter. Apart from the NEI component the model includes Galactic absorption (tbabs Wilms et al. 2000), and a power-law component to account for the X-ray synchrotron radiation. The abundances were not well constrained for all spectra, in particular for those spectra that showed evidence for a prominent synchrotron component (GM3). For that reason we made simultaneous fits to all GM spectra, coupling the abundances across all the GM spectra, but determining the other relevant parameters for each individual spectrum. We used the same procedure for the three CSM spectra. Apart from the electron temperature kT_e , τ_{\max} , the normalizations and absorption columns N_H , we also allowed for line Doppler shifts. The abundance of Ni was coupled to Fe, and the abundance of Ca was coupled to Ar. All abundances were measured in units of the Lodders et al. (2009) proto-solar abundance values.

For the optimization of the fitted model we used the Bayesian scheme employed in Ellien et al. (2023), based on the Python version of `xspec` combined with the Python package BXA (Buchner et al. 2014), a Python implementation of the `Ultraneest` algorithm (Feroz et al. 2009). The versions used in this work were `xspec` v12.13.1 and BXA v4.1.1. The `Ultraneest` algorithm ensures extensive coverage of the parameter space.

All fitted models provide reasonable fit to the spectra, given that these are line-rich spectra with excellent statistics. The latter implies that systematic uncertainties dominate. The spectra and best-fit models are shown in Fig. 2, and the best-fit parameters are listed in Table. 1.

2.2. Principal component analysis

The GM spectra are characterized by less-prominent Si-K and S-K lines as compared to ejecta spectra, which

have either bright Si-K, S-K lines, or otherwise prominent Fe-L and Fe-K line complexes (e.g. Hughes et al. 2000; Hwang & Laming 2012). However, a low equivalent width of the Si-K and S-K lines can also be caused by a dominant X-ray synchrotron component. So it is difficult from spectral fitting alone to establish whether the GM spectra are originating from metal-rich ejecta plasma, with a strong nonthermal component, or originate from CSM.

In order to better characterize the X-ray spectral content of Cas A, we resorted to a principal component analysis (PCA). PCA is a well-known statistical method in which a complex data set, represented as a set of data vectors, is restructured into a set of orthogonal eigen vectors, ordered according to their relative importance, i.e., the amount of variance they cover. PCA has been used before to characterize X-ray spectra of young SNRs, see Warren & Hughes (2004); Warren (2006).

The PCA of the data consists of representing the spatial-plus-energy data cube as a two dimensional matrix, with the rows corresponding to all the spatial pixels and the columns corresponding to discrete energy bands. For this PCA, we combined the ObsIDs 4634, 4635, 4636, 4637, 4638, 4723, creating 28 combined images (Table A1) with a pixel resolution of $0.98''$. The images were rebinned to a pixel size of at least $1.97''$ (4 by 4 Chandra pixels), using a mesh-refinement scheme common to all energy bands. The columns were centered (mean per band subtracted) and divided by the square root of the pixel variance for each band. The PCA output consists of the eigenvectors (principal components, PCs), the singular values, and the PC scores. The latter are images indicating for each pixel the amount by which it is represented by a PC.

The PC scores 2–5 are shown in Fig. A3. PC2 identifies mostly with the nonthermal X-ray emission, and PC3 and PC4 seem to identify with the (partially) iron-rich regions. PC5 appears to correlate best with some filaments associated with the GM. However, PCA regularizes data as a set of orthogonal components, whereas different physical components present in the X-ray spectra may not necessarily be orthogonal. Physical components may, therefore, be spread over different PC scores. Scatter plots of PC scores for the total data set and just the GM region (red) are shown in Fig. 3. It shows that the GM region is associated with positive values of PC2 and values of PC5 of less than 0.01.

We use these scatter plots to automatically select PC scores similar to the GM. We can identify all pixels where the spectra have similar PC properties as those of the GM. For this, we looked at the density of GM points in scatter plots like the ones shown in Fig. A3.

Table 1. Best-fit parameters for GM and CSM spectra.

Region:	GM1	GM2	GM3	GM4	GM5	CSM1	CSM2	CSM3
kT_e (keV)	$1.84^{+0.05}_{-0.05}$	$2.17^{+0.12}_{-0.12}$	$1.89^{+0.73}_{-0.73}$	$2.62^{+0.10}_{-0.10}$	$1.15^{+0.06}_{-0.06}$	$2.40^{+0.14}_{-0.14}$	$1.48^{+0.19}_{-0.19}$	$1.50^{+0.08}_{-0.08}$
O			$4.98^{+0.20}_{-0.20}$				$3.97^{+0.52}_{-0.46}$	
Ne			$2.11^{+0.14}_{-0.13}$				$1.49^{+0.14}_{-0.13}$	
Mg			$1.65^{+0.08}_{-0.08}$				$0.88^{+0.05}_{-0.05}$	
Si			$1.63^{+0.08}_{-0.08}$				$0.73^{+0.04}_{-0.04}$	
S			$1.58^{+0.09}_{-0.09}$				$0.76^{+0.05}_{-0.05}$	
Ar			$1.40^{+0.14}_{-0.13}$				$0.37^{+0.16}_{-0.11}$	
Fe			$1.39^{+0.10}_{-0.09}$				$0.94^{+0.13}_{-0.12}$	
$\tau_{\max}(10^{11} \text{ cm}^{-3} \text{ s})$	$1.29^{+0.07}_{-0.07}$	$1.83^{+0.19}_{-0.17}$	$1.12^{+0.36}_{-0.27}$	$1.08^{+0.05}_{-0.04}$	$1.85^{+0.30}_{-0.26}$	$0.60^{+0.04}_{-0.04}$	$0.71^{+0.13}_{-0.11}$	$0.78^{+0.05}_{-0.05}$
$v_{\text{rad}}(\text{km s}^{-1})$	-2.394^{+45}_{-45}	-2.634^{+99}_{-99}	-2.396^{+422}_{-422}	-2.848^{+141}_{-141}	-1.779^{+164}_{-164}	657^{+110}_{-110}	-2.544^{+257}_{-257}	-1.266^{+549}_{-549}
norm a	$4.71^{+0.34}_{-0.32}$	$1.91^{+0.13}_{-0.12}$	$0.24^{+0.04}_{-0.03}$	$3.30^{+0.24}_{-0.22}$	$1.16^{+0.10}_{-0.09}$	$1.37^{+0.09}_{-0.08}$	$0.89^{+0.09}_{-0.08}$	$3.04^{+0.14}_{-0.13}$
Γ	$3.69^{+0.04}_{-0.04}$	$2.98^{+0.04}_{-0.04}$	$2.53^{+0.04}_{-0.04}$	$3.66^{+0.02}_{-0.02}$	$3.17^{+0.28}_{-0.28}$	$3.40^{+0.15}_{-0.15}$	$3.13^{+0.29}_{-0.29}$	$2.54^{+0.31}_{-0.31}$
PL norm b	$4.26^{+0.42}_{-0.38}$	$3.38^{+0.17}_{-0.16}$	$1.22^{+0.07}_{-0.06}$	$4.20^{+0.33}_{-0.31}$	$(9.71^{+68.9}_{-8.51}) \times 10^{-6}$	$0.83^{+0.13}_{-0.11}$	$0.14^{+1.31}_{-0.13}$	$0.17^{+11.85}_{-0.17}$
$N_{\text{H}}(\text{cm}^{-2})$	$1.89^{+0.02}_{-0.02}$	$1.78^{+0.02}_{-0.02}$	$2.19^{+0.05}_{-0.05}$	$1.81^{+0.02}_{-0.02}$	$2.05^{+0.03}_{-0.03}$	$1.48^{+0.03}_{-0.03}$	$2.37^{+0.04}_{-0.04}$	$1.93^{+0.03}_{-0.03}$
C-stat/bins	261.39/83	157.34/79	90.30/75	235.28 /81	119.56 / 71	170.46/ 79	75.43/64	151.39/ 73

^a Defined as $\text{norm} = \text{EM} = 10^{-14} / (4\pi d^2) \int n_e n_{\text{H}} dV$.

^b units: $10^{-3} \text{ ph cm}^{-2} \text{ keV}^{-1} @ 1 \text{ keV}$

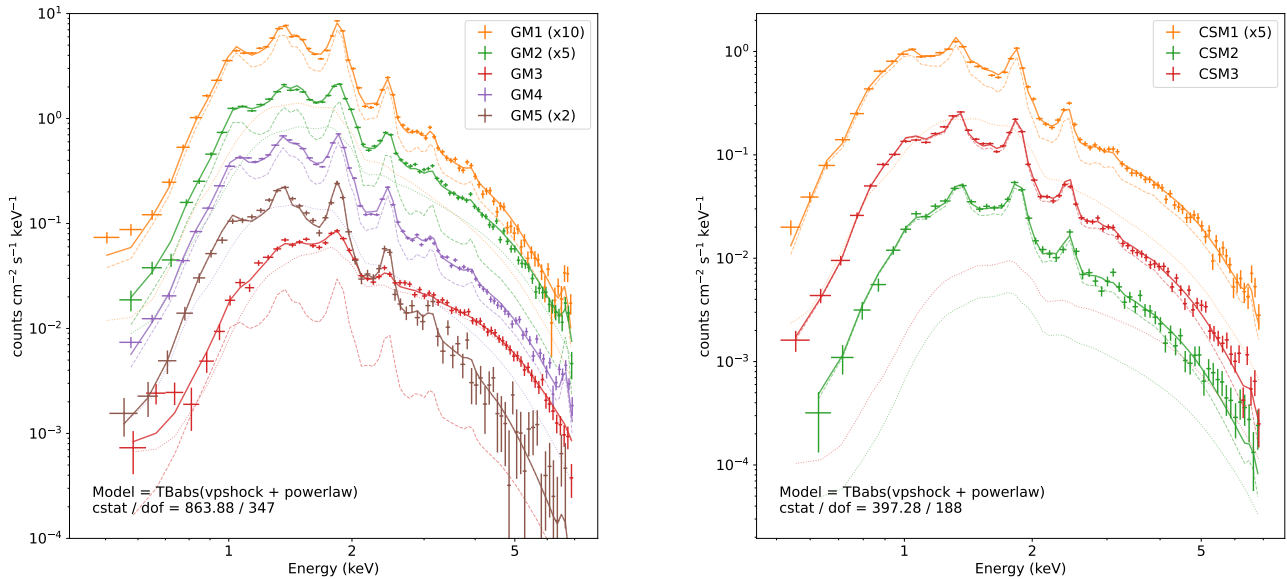


Figure 2. Left: X-ray spectra from the “Green Monster” region. Right: Spectra of the three CSM regions. See Fig. 1 and Table 1 for the identification and spectral fit parameters. The dashed and dotted lines show the model contributions of the *vpshock* and *powerlaw* components, respectively.

The selection threshold density is a tuneable parameter. Fig. 3 shows masks of all pixels where the PC1–8 properties are similar to the GM for two different selection thresholds. For the lenient threshold (Fig. 3, left), we see that the mask selects out all regions associated with the main shell, which is dominated by Si-rich ejecta emission. It also excludes the Fe-rich regions in

the southeastern part (also reddish in Fig. 1top). Instead, most of the outer regions, where we expect the shocked CSM plasma to reside, are selected. For the more stringent threshold (Fig. 3, right), some parts of the outer regions are not selected, which includes, interestingly CSM1. But the region containing the arc of QSFs in the south (CSM3) and CSM2 are shown to be

“GM-like”. Note that the threshold used here is rather severe as many areas within the GM-region itself are blacked out, perhaps due to contamination with ejecta emission or nonthermal emission.

No matter the selection threshold, the PCA analysis identifies the spectral X-ray properties of the GM to be very dissimilar from the ejecta-rich shell, and to be much more similar to regions in the outskirts of Cas A, where we expect the emission to come from shocked CSM. The dependency on threshold indicates some variations within both the GM-region as well as the outer regions of Cas A, which may be related to differences in plasma properties.

3. DISCUSSION

The GM is a striking, newly JWST/MIRI identified IR structure inside the main shell of Cas A. The JWST/MIRI data by itself already provides some clues that it is structure related to the shocked CSM. The X-ray analysis described here confirms a CSM origin. It shows that the X-ray spectra of GM regions are similar to the spectra of CSM regions, although for all these spectra there is a variable level of contribution of X-ray synchrotron radiation. A perhaps even more convincing argument that the GM X-ray spectra are CSM related is provided by a principal component analysis (PCA), which shows that the spectral properties of the GM region also identifies the outer regions of Cas A, for which the most likely origin is shocked CSM (c.f. Fig. 5 in Hwang & Laming 2012).

From the X-ray spectral analysis a few commonalities, informing us on the nature of the GM plasma, emerge:

1. the ionization ages (τ or $n_e t$) of both the GM and CSM are relatively low, $\tau_{\max} \approx 0.5\text{--}2 \times 10^{11} \text{ cm}^{-3}\text{s}$, compared to other regions of Cas A for which $\tau_{\max} > 2 \times 10^{11} \text{ cm}^{-3}\text{s}$ seems more typical (Hwang & Laming 2012);
2. the GM spectra are all blueshifted with radial velocities of $\approx -2500 \text{ km s}^{-1}$;
3. some spectra require a synchrotron contribution, which dominates the spectrum for GM3;
4. the CSM spectra are rather similar to the GM spectra in that the silicon/sulfur line emission and/or iron-line emission are much less prominent (i.e. have lower equivalent widths) than for typical spectra from Cas A (c.f. spectra in Hwang & Laming 2012).

In particular, points 1) and 4) reinforce the idea that the GM spectra are indeed CSM-related. The presence of a strong synchrotron component in some spectra (in

particular GM3) suggests that these filaments may be close to the forward shock, as the rapid synchrotron cooling times of the electrons with $\gtrsim 10 \text{ TeV}$ only allows for X-ray synchrotron radiation within 10^{17} cm of the shock (e.g. Vink & Laming 2003). But chance alignment with either forward-shock or reverse-shock-related filaments cannot be excluded.

The abundance pattern does show relatively low abundances, but are not completely consistent with solar. Optical studies indicate that the CSM of Cas A is enhanced in He and N, which will affect the thermal continuum, and hence the derived abundances of the other elements. In particular, the oxygen abundance both for the GM and the CSM spectra is relatively high. It is not clear whether the CSM of Cas A is indeed enhanced in oxygen or whether some systematics are involved. We note that oxygen is nearly completely ionized, and the low energy part of the spectrum with oxygen lines is heavily affected by absorption. Both effects may leave the measured abundance vulnerable to systematic effects. We also note that the best-fit GM abundances (except oxygen) are a factor ~ 2 higher than the CSM abundances. We caution not to over-interpret this effect. There may indeed be abundance variations throughout the CSM in Cas A, but we cannot exclude some contamination by ejecta emission to the spectra of GM regions.

The τ_{\max} values for GM regions are higher than for the CSM regions. The typically τ_{\max} values of $1.4 \times 10^{11} \text{ cm}^{-3}\text{s}$ translate into a post-shock electron density of $n_{e,1} \approx \tau_{\max}/t = 44 \text{ cm}^{-3}(t/100 \text{ yr})(\tau_{\max}/1.4 \times 10^{11})$, with t the time since the plasma was shocked. The value for τ_{\max} corresponds to a pre-shock density—i.e. a factor 4 lower—of $n_{e,0} \approx 11/(t/100 \text{ yr})(\tau_{\max}/1.4 \times 10^{11}) \text{ cm}^{-3}$. This value for the pre-shock density is a factor 5–10 higher than previous estimates (Vink 2004; Lee et al. 2014) but could be marginally consistent if one takes plasma ages closer to the maximum age of $\sim 350 \text{ yr}$.

For the CSM fits we infer still a relatively high pre-shock density of $n_{e,0} \approx 5.5/(t/100 \text{ yr})(\tau_{\max}/0.7 \times 10^{11}) \text{ cm}^{-3}$. This is a factor two lower than for the GM regions, but still higher than inferred by Lee et al. (2014). This may be caused by a bias in finding suitable CSM extraction regions, for which we focussed on clear structures, rather than very diffuse regions.

The blueshifts of the GM spectra indicate that the GM lies on the near-side of Cas A, and, as shown in Fig. A2, are statistically significant. Interestingly, the QSF regions are also on average blueshifted, with optically determined Doppler shifts of approximately $-600\text{--}100 \text{ km s}^{-1}$ (van den Bergh 1971; Alarie et al. 2014).

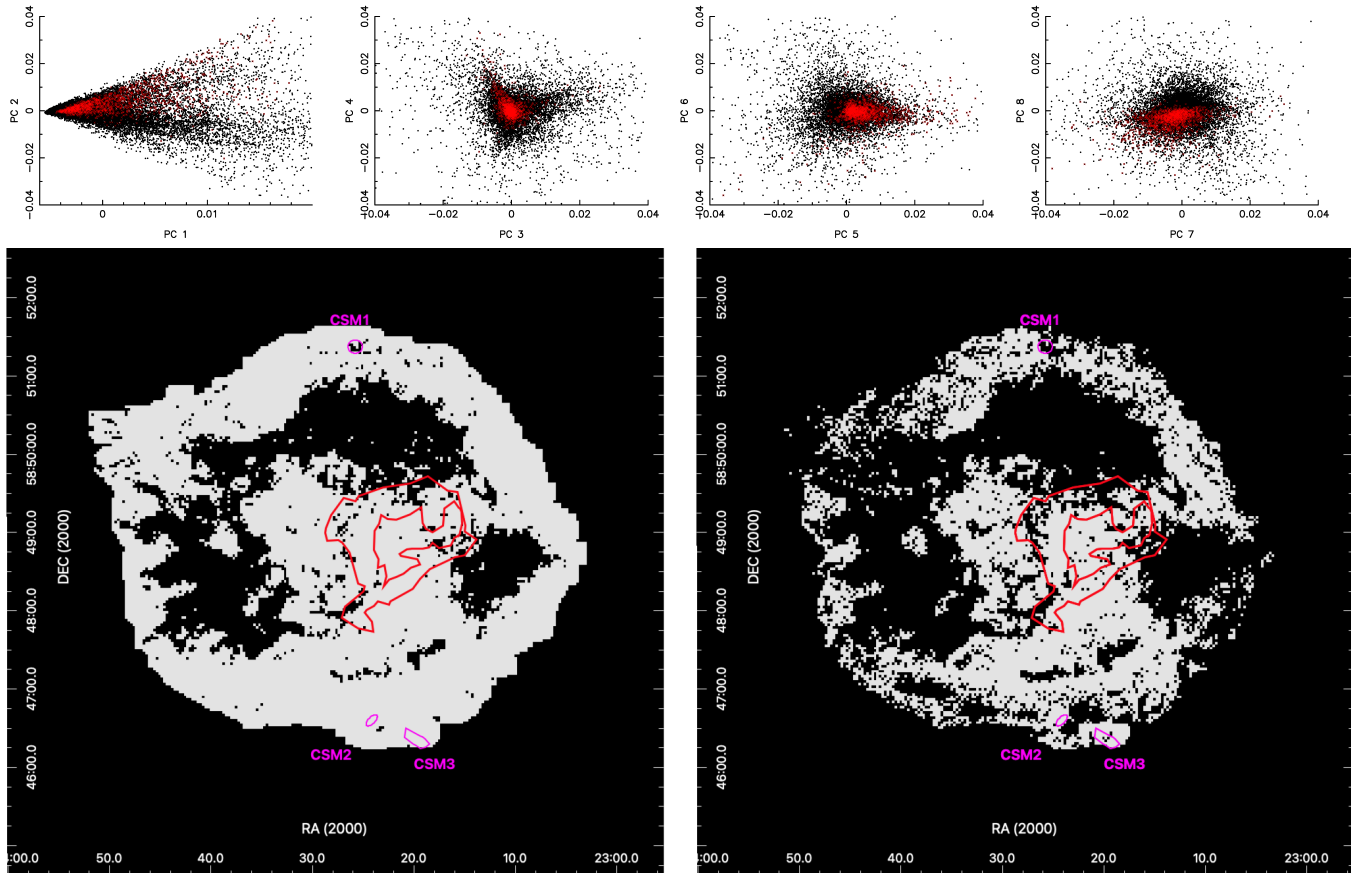


Figure 3. Top panels: Scatterplot of PC scores for all pixels (black) and those corresponding to the GM region (red), zooming in on where the majority of the points are located. (See Fig. A4 for the full range of PC scores.) Bottom panels: Mask created from the PC1 to PC8 scores using values corresponding to the red colored regions in the top panels. The left panel corresponds to a loose selection and the right panel to a more stringent selection (see text).

Another hint that there may be a connection between the QSFs and the GM (c.f. De Looze et al.).

The regions CSM2 and CSM3 analyzed here, are associated with the QSFs, and appear also blueshifted, indicating surprisingly large radial velocities. CSM3, at the tip of the arc of QSFs, may, in fact, have a smaller Doppler shift than tabulated: the Doppler shift probability density distribution (Fig. A2) shows two peaks of high likelihood, of which one is being consistent with no Doppler shift. The blueshift of $\sim 2500 \text{ km s}^{-1}$ for CSM2 is statistically significant. This could be possible if locally the shock velocity is large and the X-ray emitting plasma received a relatively large velocity. CSM2 is located in a region where the measured X-ray proper motions indicate that the shock velocity changes from $\sim 6200 \text{ km s}^{-1}$ to $\sim 4000 \text{ km s}^{-1}$ (Vink et al. 2022). So a high shock velocity around CSM2 may indeed be possible, but needs to be further investigated.

CSM1 is not associated with QSFs, and is the only region analyzed here that shows a redshift rather than a blueshift.

The typical GM's radial velocity of $|v_{\text{rad}}| = 2500 \cos i \text{ km s}^{-1}$ corresponds to shock velocities of $V_s \approx 3300 \cos i \text{ km s}^{-1}$, given that the plasma downstream of a strong shock running into a monatomic gas has $v_{\text{plasma}} = 4/3V_s$. The factor $\cos i$ takes into account projection effects. Since the GM lies close to the center, the projection effects should be small — $\cos i \approx 0-30^\circ$ — which suggests that the GM is associated with parts of the CSM where the shock front has decelerated to $V_s \sim 3500-4000 \text{ km s}^{-1}$. X-ray proper motion studies of Cas A show that the typical shock speeds are 5800 km s^{-1} (Vink et al. 2022). But a value as low as 4038 km s^{-1} is reported for a position angle of 190° . Interestingly, this corresponds to the region containing the arc of QSFs, for which a higher than average density is likely. Since the shock velocities for a given postshock pressure are proportional to $\rho_0 V_s^2$, we expect that the lower inferred shock velocities are the result of a pre-shock density that is $V_{s,\text{GM}}^2/\overline{V_s}^2 \approx 3$ higher than the average CSM density near the current shock front. So both the best-fit τ_{max} values, as well as the relatively low

plasma velocities of $\approx 2500 \text{ km s}^{-1}$ suggest that the filaments in the GM stand out due to a higher than average density.

Some of the X-ray analysis presented here goes beyond the main topic of this paper, i.e. the nature of the GM. For example, the PCA provides a yet unexplored way to identify which parts of Cas A consist mostly of shocked CSM and which parts consist of shocked ejecta. It is interesting that most of the region interior to the main shell—not just the GM—seems to be spectroscopically similar to the shocked CSM. This suggests a lack of ejecta-related emission from the central regions of Cas A. According to the PCA CSM1 appears to have different X-ray properties than the GM regions and CSM2 and CSM3, which may reflect some reveal variation in thermal X-ray emission from the shocked CSM. This may be related to the variation in IR dust grain emission properties between the northern CSM on the one hand, and the QSF and GM-related emission on the other hand, which is due to a higher carbon-over-silicate abundance in the QSF and GM regions (De Looze et al.).

Another noteworthy result of the PCA is that the main shell for position angles between roughly 170° and 200° seems to have some CSM-like properties, except for two narrow gaps. This is a region in which the ejecta shell is relatively narrow in X-rays (Fig. 1top) and in the optical the ejecta-related fast moving knots only started appearing since the 1970s (see Fig. 1 in Patnaude & Fesen 2014). Some of the IR emission properties in that region seem to be similar to the GM emission (Milisavljevic et al., De Looze et al.). In addition, this region is also relatively bright in [Fe II] $1.644 \mu\text{m}$, which it has in common with the arc of QSFs further to the south (Lee et al. 2017, their Fig. 12). Lee et al. (2017) attribute this to a prominent CSM component associated with the contact discontinuity in this part of the shell.

4. CONCLUSION

We analyzed the X-ray properties of the JWST-identified “Green Monster” (GM) region in order to study the nature of this new structure. For the X-ray investigation, we used a spectral analysis employing an absorbed `vpshock` plus power-law model, the latter to account for nonthermal X-ray emission. For optimizing the models we used a Bayesian analysis scheme. In addition, we characterized the X-ray spectral properties of the GM in comparison to the rest of Cas A using PCA.

Both types of X-ray analysis suggest that the GM is a structure that has similar spectral characteristics as the outer regions of Cas A, which consist most likely of shocked CSM. For the PCA this conclusion is based on the fact that selecting PC scores associated with the GM also select for the outer regions of Cas A, and exclude the Si-rich and Fe-rich ejecta components. Spectroscopically we show that that GM spectra are relatively weak in Si XIII emission—and line emission from other intermediate mass elements—and are well characterized by abundances that are close to solar abundances, and quite similar to other CSM-related spectra.

The analysis presented here supports the conclusion of De Looze et al., based on JWST data alone, that the GM monster structure corresponds to a structure in the CSM of Cas A, rather than to a ejecta-related structure.

In addition, the X-ray analysis shows that the GM spectra are blueshifted by about 2500 km s^{-1} , suggesting that the GM structure is on the near-side of Cas A, and projected onto the interior. The radial velocity is relatively low, given the average shock speed of Cas A of 5800 km s^{-1} , which could be explained if the pre-shock CSM corresponding to the GM was a factor 2–3 denser than the average CSM density.

The infrared and X-ray properties of the GM provide yet another piece of the puzzle regarding the CSM of Cas A. This will help to reconstruct the mass-loss properties of the progenitor star, and how it ended up to become the Type IIb supernova identified from light echo spectra (Krause et al. 2008; Rest et al. 2011).

- 1 The authors thank the Lorentz Center Leiden and the
- 2 main scientific organizer Maria Arias for organizing the
- 3 workshop “Supernova remnants in complex environ-
- 4 ments”, where most of the authors were present. We
- 5 thank Amaël Ellien and Emanuele Greco for helping
- 6 M.A. set up the Bayesian spectral fitting procedures,
- 7 and we thank Alessandra Mercuri for her help in un-
- 8 derstanding the X-ray properties of the shocked CSM
- 9 in Cas A. M.A. is supported by the research program
- 10 Athena with project No. 184.034.002, which is (par-
- 11 tially) financed by the Dutch Research Council (NWO).
- 12 J.V. is supported by funding from the European Unions
- 13 Horizon 2020 research and innovation program under
- 14 grant agreement No. 101004131 (SHARP). D.M. ac-
- 15 knowledges NSF support from grants PHY- 2209451 and
- 16 AST-2206532.

REFERENCES

- Alarie, A., Bilodeau, A., & Drissen, L. 2014, MNRAS, 441, 2996, doi: [10.1093/mnras/stu774](https://doi.org/10.1093/mnras/stu774)
- Arnaud, K. A. 1996, Astronomical Society of the Pacific Conference Series, Vol. 101, XSPEC: The First Ten Years, 17

- Baade, W., & Minkowski, R. 1954, *ApJ*, 119, 206, doi: [10.1086/145812](https://doi.org/10.1086/145812)
- Blackburn, J. K. 1995, in *Astronomical Society of the Pacific Conference Series*, Vol. 77, *Astronomical Data Analysis Software and Systems IV*, ed. R. A. Shaw, H. E. Payne, & J. J. E. Hayes, 367
- Borkowski, K. J., Rho, J., Reynolds, S. P., & Dyer, K. K. 2001, *ApJ*, 550, 334, doi: [10.1086/319716](https://doi.org/10.1086/319716)
- Braun, R. 1987, *A&A*, 171, 233. <https://ui.adsabs.harvard.edu/abs/1987A&A...171..233B>
- Buchner, J., Georgakakis, A., Nandra, K., et al. 2014, *A&A*, 564, A125, doi: [10.1051/0004-6361/201322971](https://doi.org/10.1051/0004-6361/201322971)
- Ellien, A., Greco, E., & Vink, J. 2023, *ApJ*, 951, 103, doi: [10.3847/1538-4357/accc85](https://doi.org/10.3847/1538-4357/accc85)
- Feroz, F., Hobson, M. P., & Bridges, M. 2009, *MNRAS*, 398, 1601, doi: [10.1111/j.1365-2966.2009.14548.x](https://doi.org/10.1111/j.1365-2966.2009.14548.x)
- Gotthelf, E. V., Koralesky, B., Rudnick, L., et al. 2001, *ApJL*, 552, L39, doi: [10.1086/320250](https://doi.org/10.1086/320250)
- Helder, E. A., & Vink, J. 2008, *ApJ*, 686, 1094, doi: [10.1086/591242](https://doi.org/10.1086/591242)
- Hughes, J. P., Rakowski, C. E., Burrows, D. N., & Slane, P. O. 2000, *ApJL*, 528, L109, doi: [10.1086/312438](https://doi.org/10.1086/312438)
- Hwang, U., & Laming, J. M. 2012, *ApJ*, 746, 130, doi: [10.1088/0004-637X/746/2/130](https://doi.org/10.1088/0004-637X/746/2/130)
- Hwang, U., et al. 2004, *ApJL*, 615, L117, doi: [10.1086/426186](https://doi.org/10.1086/426186)
- Kaastra, J. S., & Bleeker, J. A. M. 2016, *A&A*, 587, A151, doi: [10.1051/0004-6361/201527395](https://doi.org/10.1051/0004-6361/201527395)
- Koo, B.-C., Kim, D., Yoon, S.-C., & Raymond, J. C. 2023, *ApJ*, 945, 158, doi: [10.3847/1538-4357/acb7e7](https://doi.org/10.3847/1538-4357/acb7e7)
- Koo, B.-C., Kim, H.-J., Oh, H., et al. 2020, *Nature Astronomy*, 4, 584, doi: [10.1038/s41550-019-0996-4](https://doi.org/10.1038/s41550-019-0996-4)
- Krause, O., Birkmann, S. M., Usuda, T., et al. 2008, *Science*, 320, 1195, doi: [10.1126/science.1155788](https://doi.org/10.1126/science.1155788)
- Lee, J.-J., Park, S., Hughes, J. P., & Slane, P. O. 2014, *ApJ*, 789, 7, doi: [10.1088/0004-637X/789/1/7](https://doi.org/10.1088/0004-637X/789/1/7)
- Lee, Y.-H., Koo, B.-C., Moon, D.-S., Burton, M. G., & Lee, J.-J. 2017, *ApJ*, 837, 118, doi: [10.3847/1538-4357/aa60c0](https://doi.org/10.3847/1538-4357/aa60c0)
- Lodders, K., Palme, H., & Gail, H. P. 2009, *Landolt Börnstein*, 4B, 712, doi: [10.1007/978-3-540-88055-4_34](https://doi.org/10.1007/978-3-540-88055-4_34)
- Patnaude, D. J., & Fesen, R. A. 2014, *ApJ*, 789, 138, doi: [10.1088/0004-637X/789/2/138](https://doi.org/10.1088/0004-637X/789/2/138)
- Patnaude, D. J., Vink, J., Laming, J. M., & Fesen, R. A. 2011, *ApJL*, 729, L28+, doi: [10.1088/2041-8205/729/2/L28](https://doi.org/10.1088/2041-8205/729/2/L28)
- Rest, A., Foley, R. J., Sinnott, B., et al. 2011, *ApJ*, 732, 3, doi: [10.1088/0004-637X/732/1/3](https://doi.org/10.1088/0004-637X/732/1/3)
- Uchiyama, Y., & Aharonian, F. A. 2008, *ApJL*, 677, L105, doi: [10.1086/588190](https://doi.org/10.1086/588190)
- van den Bergh, S. 1971, *ApJ*, 165, 457, doi: [10.1086/150913](https://doi.org/10.1086/150913)
- Vink, J. 2004, *New Astronomy Review*, 48, 61, doi: [10.1016/j.newar.2003.11.008](https://doi.org/10.1016/j.newar.2003.11.008)
- Vink, J., & Laming, J. M. 2003, *ApJ*, 584, 758, doi: [10.1086/345832](https://doi.org/10.1086/345832)
- Vink, J., Patnaude, D. J., & Castro, D. 2022, *ApJ*, 929, 57, doi: [10.3847/1538-4357/ac590f](https://doi.org/10.3847/1538-4357/ac590f)
- Warren, J. S. 2006, PhD thesis, Rutgers University, New Jersey
- Warren, J. S., & Hughes, J. P. 2004, *ApJ*, 608, 261
- Wilms, J., Allen, A., & McCray, R. 2000, *ApJ*, 542, 914, doi: [10.1086/317016](https://doi.org/10.1086/317016)

APPENDIX

SUPPLEMENTARY MATERIAL

This appendix shows supplementary material that support the main text. Fig. A1 identifies several regions of interest, mentioned in the text. Fig. A2 provides the sampling plots for the spectral fits for the Doppler shift parameters versus τ_{\max} . Table A1 shows the image energy bands used for the PCA. The first eight PCA score images are shown in Fig. A3.

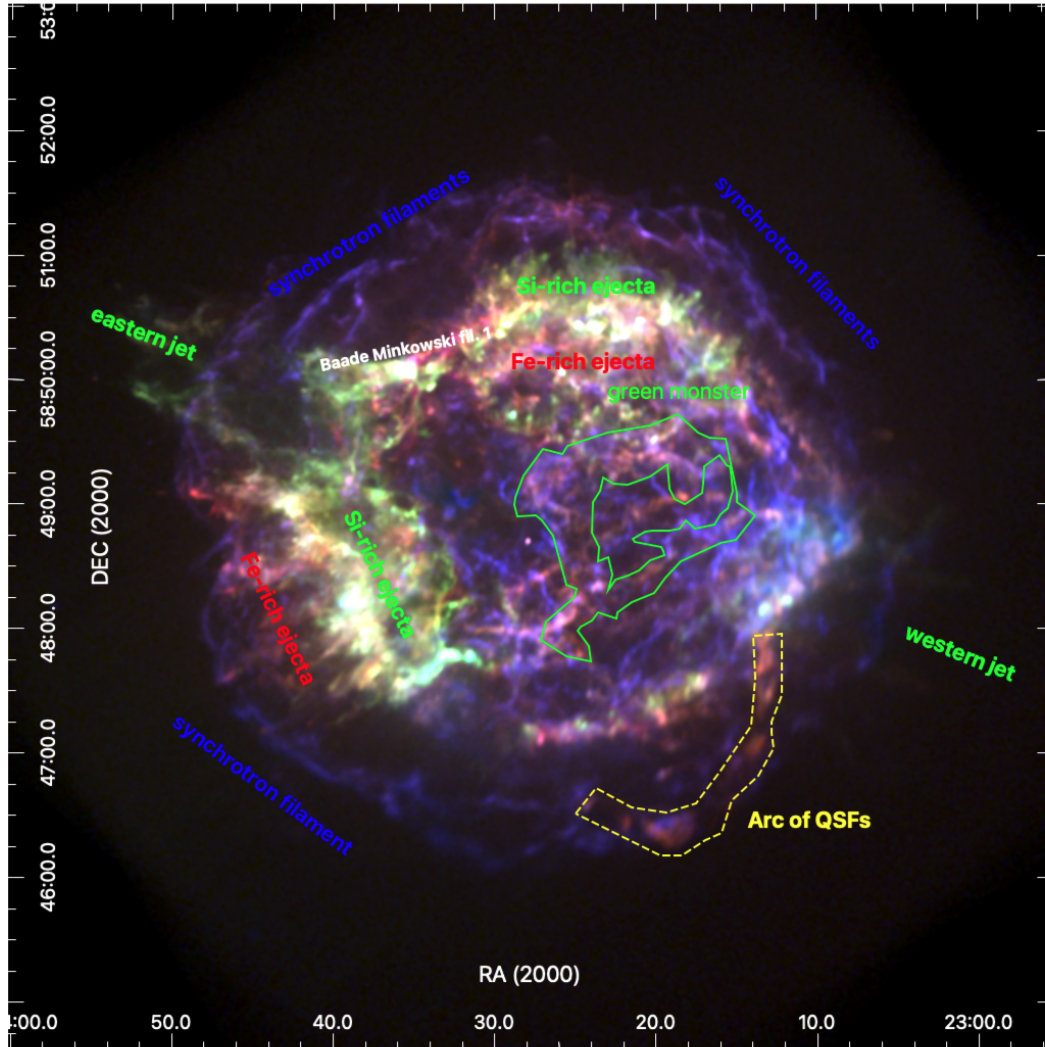


Figure A1. Same as Fig. 1, but now with rough indications of important regions mentioned in the text. In general, all Si-rich ejecta show up here in green. Fe-rich ejecta show up as shades of red, but so are regions relatively abundant in Ne IX/X and Mg XI/XII. Bright X-ray synchrotron filaments show up in shades of purple.

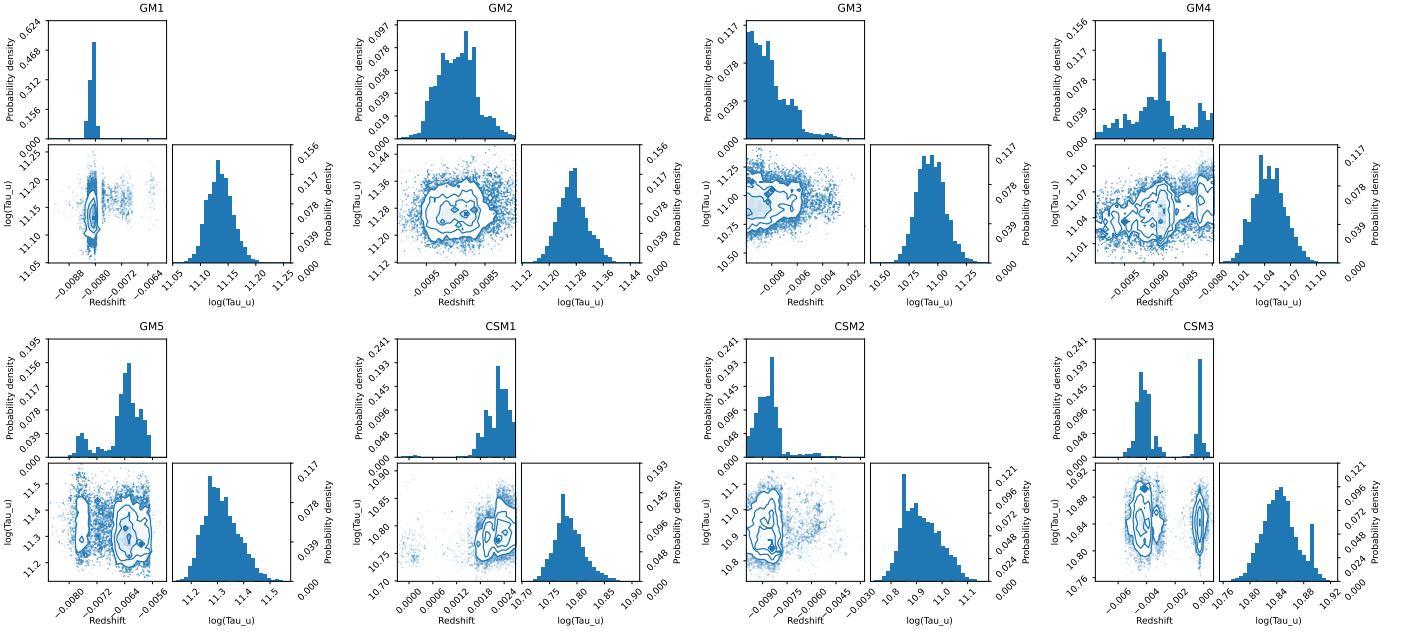


Figure A2. Correlation plots of the Doppler shifts versus τ_{\max} for all GM and CSM regions. The histograms are normalized to a sum of one to form a probability density distribution. The GM analysis is based on 128263 nested sampling iterations and for the CSM analysis there were 41480 nested sampling iterations.

Table A1. Input energy bands used for principal component analysis.

	E_{\min} (keV)	E_{\max} (keV)		E_{\min} (keV)	E_{\max} (keV)
1	0.50	0.62	15	2.63	2.78
2	0.62	0.72	16	2.78	3.00
3	0.72	0.87	17	3.00	3.28
4	0.87	1.03	18	3.28	3.60
5	1.03	1.12	19	3.60	3.75
6	1.12	1.23	20	3.75	4.04
7	1.23	1.42	21	4.04	4.50
8	1.42	1.56	22	4.50	5.00
9	1.56	1.69	23	5.00	5.40
10	1.69	1.85	24	5.40	5.75
11	1.85	1.98	25	5.75	6.25
12	1.98	2.13	26	6.25	6.62
13	2.13	2.28	27	6.62	6.85
14	2.28	2.63	28	6.85	7.35

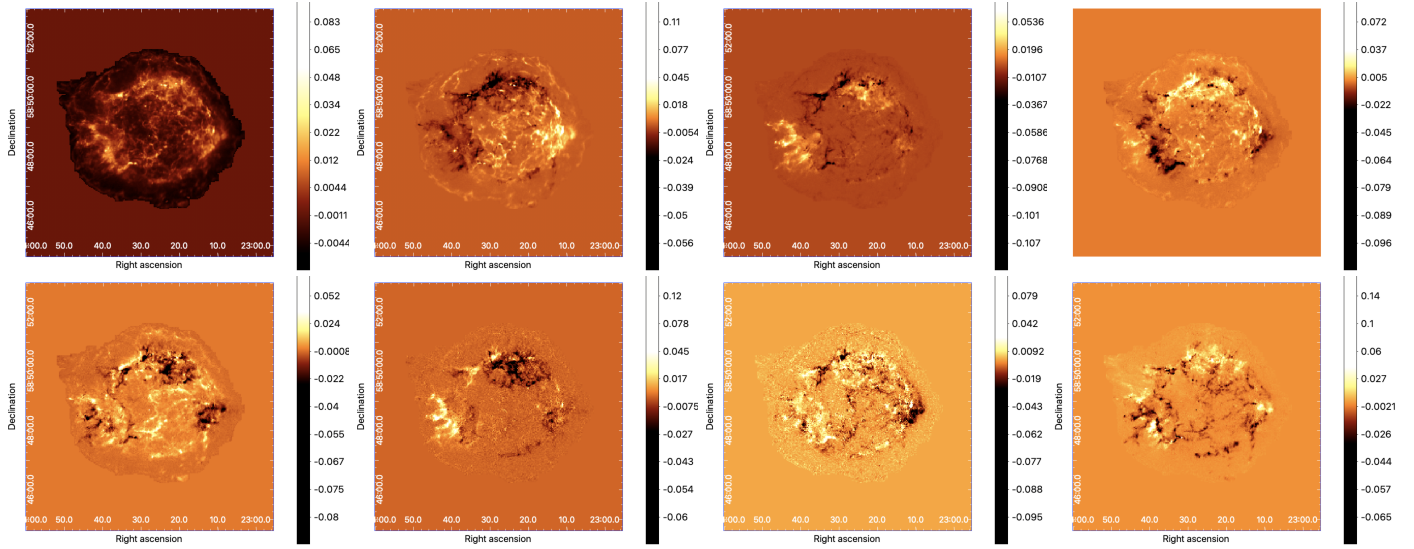


Figure A3. The PC scores 1 (top left) to 8 (bottom right). In particular in the scores for PC 5, 7, 8 one recognizes some of the filaments associated with the GM.

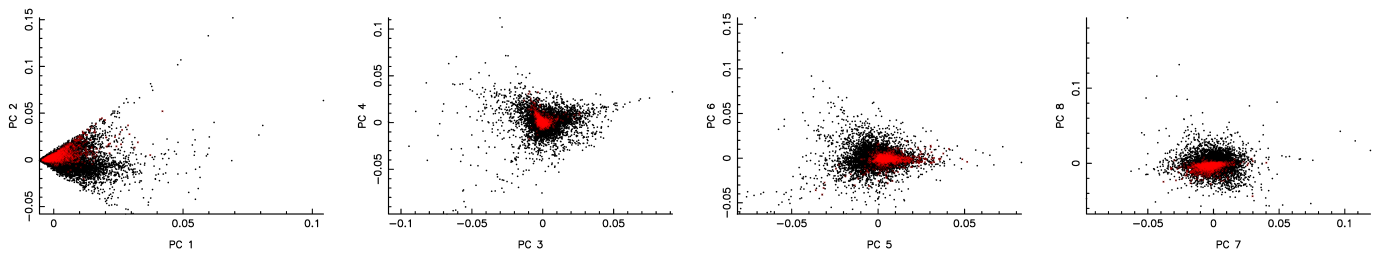


Figure A4. Same as top panels of Fig. 3, but now with the full range of PC scores.